

Strongly interacting Hofstadter states in magic-angle twisted bilayer graphene

In the format provided by the
authors and unedited

Table of contents

Note S1. Self-consistent Hartree-Fock calculation of MATBG at finite field.

Note S2. Quantum geometry properties of the FQHs and the FCI indicators.

Note S3. Orbital decomposition of the magnetic subbands.

Figure S1. Temperature dependence of the resistivity ρ_{xx} at zero magnetic field.

Figure S2. Filling factor dependence of AHE near $\nu = 1$ and 2.

Figure S3. Landau Fan diagram in Hall resistivity ρ_{yx} and other contact pairs.

Figure S4. Landau Fan diagrams in ρ_{xx} and ρ_{yx} at $T = 2$ K.

Figure S5. Landau Fan diagrams in ρ_{yx} of the SBCIs.

Figure S6. Temperature dependence of the SBCIs.

Figure S7. Observation of SBCIs at electron doping side.

Figure S8. Flavor symmetry of the main sequence Correlated Chern insulators with $(t, s) = (-1, -3), (-2, -2), (-3, -1)$.

Figure S9. Calculation of the flavor symmetry of the $t = 0$ IKS states at finite magnetic field.

Figure S10. Interacting Hofstadter spectrum of the half-integer SBCIs.

Figure S11. Local density of states at the conduction band edge of the $(-3, -1/2)$ SBCI.

Figure S12. Finite-field Hartree-Fock calculation at twist angle 1.03° .

Figure S13. Finite-field Hartree-Fock calculation at twist angle 1.05° with presence of SOC.

Figure S14. Calculation of the flavor and magnetic translation symmetry of the SBCI states at finite magnetic field.

Figure S15. Temperature dependence of the FQHs.

Figure S16. FQHs and Fermi liquid at high magnetic field.

Figure S17. Orbital decomposition of the magnetic subband.

Figure S18. Comparison of the quantum geometry conditions with and without Coulomb interaction.

We first briefly summarize the conventions used in this work for constructing the finite magnetic field phase diagram based on the interacting Bistritzer-MacDonald (BM) model in the presence of uniaxial heterostrain, the procedure for calculating the STM local density of states (LDOS), as well as the fractional Chern insulator (FCI) indicators of interaction-renormalized magnetic subbands. For more detailed discussions we refer interested readers to the Supplementary Information (SI) in Ref. [1].

Conventions

Uniaxial heterostrain refers to applying uniaxial tensile strain to one layer of graphene, and compressive strain of equal strength along the same axis to the other layer. It is parameterized by the heterostrain strength ϵ and orientation φ . We define the orientation with respect to the zigzag edge of untwisted and undeformed monolayer graphene. The impact of uniaxial heterostrain is amplified on the moiré length scale, causing deformations of the moiré (reciprocal) lattice vectors as well as modifying the energy dispersions of the moiré flat bands [2,3]. We hereby use the notations $\mathbf{L}_{i=1,2}$ to denote the deformed moiré lattice vectors, and $\mathbf{g}_{i=1,2}$ to denote the deformed reciprocal lattice vectors after the application of strain. They satisfy $\mathbf{L}_i \cdot \mathbf{g}_j = 2\pi\delta_{ij}$. We also use the convention that the top (bottom) graphene layer is twisted counterclockwise (clockwise) by $\theta/2$, and define the $+\hat{z}$ direction along the out-of-plane axis from the bottom layer to the top layer.

In a finite magnetic field along the $+\hat{z}$ direction $\mathbf{B} = B\hat{z}$, the BM model of a given valley ($\eta = \mathbf{K}, \mathbf{K}'$) and spin ($s = \uparrow, \downarrow$) flavor, $\hat{H}_{\eta,s}(\hat{\mathbf{p}})$, is modified to $\hat{H}_{\eta,s}(\hat{\mathbf{p}} + e\mathbf{A}(\mathbf{r}))$, where $\hat{\mathbf{p}} \equiv -i\hbar\nabla$ is the momentum, $e > 0$ is the absolute charge of an electron, and $\mathbf{A}(\mathbf{r})$ is the magnetic vector potential satisfying $\nabla \times \mathbf{A}(\mathbf{r}) = \mathbf{B}$. We shall choose the Landau gauge $\mathbf{A}(\mathbf{r}) \equiv Bx\hat{\mathbf{y}}$ where the $\hat{\mathbf{y}}$ is defined to be along the strain-deformed \mathbf{L}_2 .

Note S1. Self-consistent Hartree-Fock calculation of MATBG at finite field.

The finite magnetic field studies are performed at rational magnetic flux ratios $\phi/\phi_0 = p/q$ where $\{p, q\}$ are coprime integers, $\phi = \mathbf{B} \cdot (\mathbf{L}_1 \times \mathbf{L}_2)$ is the flux per moiré unit cell, and $\phi_0 = h/e$ is the magnetic flux quantum. At these flux ratios, the interacting BM model preserves the magnetic translation symmetry generated by

$$\hat{t}_{\mathbf{L}_1}(\mathbf{r}) \equiv e^{-i2\pi\frac{\phi}{\phi_0}\left(\frac{y}{|\mathbf{L}_2|} - \frac{\mathbf{L}_{1y}}{2|\mathbf{L}_2|}\right)} \hat{T}_{\mathbf{L}_1}, \quad \hat{t}_{\mathbf{L}_2} \equiv \hat{T}_{\mathbf{L}_2},$$

with $\hat{T}_{\mathbf{L}_{i=1,2}}$ the discrete moiré translations at $B = 0$. The magnetic translation operators do not commute $[\hat{t}_{\mathbf{L}_1}(\mathbf{r}), \hat{t}_{\mathbf{L}_2}] \neq 0$, however they satisfy $[\hat{t}_{\mathbf{L}_1}(\mathbf{r}), \hat{t}_{\mathbf{L}_2}^q] = 0$. Therefore, to study the finite B problem we enlarge the unit cell to be $\mathbf{L}_1 \times q\mathbf{L}_2$. Accordingly, we can define ‘‘magnetic Bloch states’’ labeled by the magnetic wavevector $\mathbf{k} = k_1\mathbf{g}_1 + k_2\mathbf{g}_2$, where $k_1 \in [0,1]$ and $k_2 \in [0,1/q]$. The magnetic Bloch states $|\Psi_a^{(\eta s)}(\mathbf{k})\rangle$ are constructed from the monolayer Landau level wavefunctions, with more details presented in Ref. [1]. They are labeled by the magnetic subband index $a = 1, \dots, 2q$, and we order these states by increasing energy of the non-interacting BM model. In contrast to $B = 0$, here there are $2q$ magnetic subbands per valley and spin instead

of 2. However, the magnetic Brillouin zone is also q times smaller, therefore preserving the dimension of the Hilbert space between $B = 0$ and $B \neq 0$.

The interacting BM model projected onto the narrow moiré bands can be written as follows:

$$H = \sum_{\eta s \mathbf{k}} \varepsilon_a^{(\eta s)}(\mathbf{k}) d_{\eta s a, \mathbf{k}}^\dagger d_{\eta s a, \mathbf{k}} + \frac{1}{2A} \sum_{\mathbf{q}} V_{\mathbf{q}} \delta \hat{\rho}_{\mathbf{q}} \delta \hat{\rho}_{-\mathbf{q}},$$

where $d_{\eta s a, \mathbf{k}}$ is the electron annihilation operator and $\varepsilon_a^{(\eta s)}(\mathbf{k})$ is the dispersion of the magnetic subband indexed by a . The projected density operator subtracting a background charge is given by:

$$\delta \hat{\rho}_{\mathbf{q}} = \sum_{\eta s, ab, \mathbf{k}} \langle \Psi_a^{(\eta s)}(\mathbf{k}) | e^{-i\mathbf{q} \cdot \mathbf{r}} | \Psi_b^{(\eta s)}(\mathbf{k} + \mathbf{q}) \rangle \left(d_{\eta s a, \mathbf{k}}^\dagger d_{\eta s b, \mathbf{k} + \mathbf{q}} - \frac{1}{2} \delta_{\mathbf{q}, \mathbf{G}} \delta_{a, b} \right),$$

where $\mathbf{G} = m\mathbf{g}_1 + n\mathbf{g}_2$, $\{m, n\} \in \mathbb{Z}$. In the literature the coefficient due to projection is referred to as the structure factor $\hat{\Lambda}_{\mathbf{q}}^{(\eta s)}(\mathbf{k})$, and can be equivalently denoted as:

$$[\hat{\Lambda}_{\mathbf{q}}^{(\eta s)}(\mathbf{k})]_{a, b} \equiv \langle \Psi_a^{(\eta s)}(\mathbf{k}) | e^{-i\mathbf{q} \cdot \mathbf{r}} | \Psi_b^{(\eta s)}(\mathbf{k} + \mathbf{q}) \rangle \equiv \langle u_a^{(\eta s)}(\mathbf{k}) | u_b^{(\eta s)}(\mathbf{k} + \mathbf{q}) \rangle,$$

where $|u_a^{(\eta s)}(\mathbf{k})\rangle$ is the magnetic unit cell periodic part of the magnetic Bloch state. A is the total area of the system, and $V_{\mathbf{q}} = \frac{2\pi e^2}{\epsilon_0 \epsilon_r} \frac{\tanh(|\mathbf{q}| \xi / 2)}{|\mathbf{q}|}$ is the dual gate screened Coulomb interaction.

The parameters for the theoretical calculations in the main text is as follows: twist angle $\theta = 1.05^\circ$, uniaxial heterostrain strength $\epsilon = 0.2\%$ and orientation $\varphi = 0^\circ$, monolayer graphene Fermi velocity $v_F = 9.264 \times 10^5 \text{ m/s}$, interlayer tunneling parameters $w_0 = 77 \text{ meV}$ and $w_1 = 110 \text{ meV}$, relative dielectric constant $\epsilon_r = 15$, and screening length $\xi = 4\sqrt{|L_1||L_2|} \approx 52 \text{ nm}$. Lattice relaxation effects are neglected in this calculation. For details of the self-consistent Hartree-Fock method we refer readers to SI of Ref. [1]. Most generally, our Hartree-Fock procedure can probe Slater determinant states given by the following equation:

$$|\Omega_{\text{HF}}\rangle = \prod'_{n, \mathbf{k}} \left(\sum_{sa} \alpha_{sa, \mathbf{k}}^{(n)} d_{Ksa, \mathbf{k}}^\dagger + \sum_{s'a'} \beta_{s'a', \mathbf{k} + \mathbf{q}_0}^{(n)} d_{K's'a', \mathbf{k} + \mathbf{q}_0}^\dagger \right) |0\rangle,$$

where $\Pi'_{n, \mathbf{k}}$ is a constrained product over all occupied single-electron eigenstates $\{n, \mathbf{k}\}$ of the Hartree-Fock Hamiltonian. \mathbf{q}_0 is an arbitrary wavevector shift between single electron states in opposite valleys, and $\{\alpha_{sa, \mathbf{k}}^{(n)}, \beta_{s'a', \mathbf{k} + \mathbf{q}_0}^{(n)}\}$ are variational parameters satisfying $\sum_{sa} |\alpha_{sa, \mathbf{k}}^{(n)}|^2 + \sum_{s'a'} |\beta_{s'a', \mathbf{k} + \mathbf{q}_0}^{(n)}|^2 = 1$ for any $\{n, \mathbf{k}\}$. The Hartree-Fock Hamiltonian is minimized with respect to both $\{\alpha_{sa, \mathbf{k}}^{(n)}, \beta_{s'a', \mathbf{k} + \mathbf{q}_0}^{(n)}\}$ and \mathbf{q}_0 . The latter gives the variational freedom to probe intervalley Kekulé spiral ordered (IKS) states as well as other translation symmetry breaking states such as the symmetry-broken Chern insulator (SBCI). We hereby define the one-particle density matrix:

$$[\hat{P}(\mathbf{k})]_{\eta s a, \eta' s' a'} = \langle d_{\eta s a, \mathbf{k}}^\dagger d_{\eta' s' a', \mathbf{k} + \mathbf{q}_0} \rangle.$$

Its diagonal matrix elements denote the occupation number of a given electronic state. For an IKS state [4] the density matrix also satisfies the condition:

$$\hat{t}_{\mathbf{L}_2} [\hat{P}(\mathbf{k})]_{\eta s a, \eta' s' a'} \hat{t}_{\mathbf{L}_2}^{-1} = e^{i\varphi(\eta - \eta')} \left[\hat{P} \left(\mathbf{k} + \frac{\phi}{\phi_0} \mathbf{g}_1 \right) \right]_{\eta s a, \eta' s' a'}.$$

where an IKS state constrains φ to be an arbitrary real number, see SI III. D of Ref [1] for details.

Inclusion of spin-orbit coupling

The above formalism applies in the absence of spin-orbit coupling (SOC). In the presence of SOC, and in particular the Rashba term, spin is no longer a good quantum number. The above discussions hold by combining the spin (s) and magnetic subband (a) quantum numbers into one quantum number denoting spin-hybridized magnetic subbands ($\tilde{a} = 1, 2, \dots, 4q$).

STM Local Density of States (LDOS)

Here we present a calculation of the LDOS in finite magnetic field shown in Fig. 3 of the main text and Fig. S11 of the Supplementary Information, which would be relevant for STM experiments. We denote the eigenbasis of the Hartree-Fock mean field Hamiltonian and its single particle eigenenergies as: $\{|\Gamma_{n,\mathbf{k}}\rangle, E_{n,\mathbf{k}}\}$. The LDOS at a given energy μ is therefore given by [5]:

$$\mathcal{N}(\mu, \mathbf{r}) \propto \sum_{n,\mathbf{k}} \delta(\mu - E_{n,\mathbf{k}}) |\langle \mathbf{r} | \Gamma_{n,\mathbf{k}} \rangle|^2.$$

Here the LDOS does not resolve the sublattice and layers. The real space wavefunction is related to the magnetic Bloch states via a unitary transformation:

$$\langle \mathbf{r} | \Gamma_{n,\mathbf{k}} \rangle = \sum_{\eta s a} U_{\eta s a, n}(\mathbf{k}) \langle \mathbf{r} | \Psi_a^{(\eta s)}(\mathbf{k}) \rangle,$$

and the real space wavefunction of the magnetic Bloch states can be calculated from the monolayer graphene Landau level basis states (see SI of Ref. [1]). In computing the LDOS maps for SBCIs in the main text, we approximated $\delta(\mu - E_{n,\mathbf{k}}) \approx \frac{1}{\pi} \frac{\gamma}{(\mu - E_{n,\mathbf{k}})^2 + \gamma^2}$, with an energy broadening factor $\gamma = 0.5 \text{ meV}$. In Fig. 3 and Fig. S11, the LDOS are plotted using an effective periodicity of the strained moiré superlattice, $a_M \equiv \sqrt{|\mathbf{L}_1| |\mathbf{L}_2|}$.

Note S2. Quantum geometry properties of the FQHs and the FCI indicators.

The experimentally observed fractional quantum Hall states (FQHs) emanate from the charge neutrality point (CNP), and importantly require a critical field of around 4 Tesla to occur. The latter condition places the observations in the Hofstadter regime when the magnetic length is comparable to the moiré length scale, in sharp contrast to FQHs emanating from a single Landau level. The dissimilarity between the (interaction-renormalized) magnetic subbands and single LLs is demonstrated by computing the Berry curvature and quantum geometry variations in the magnetic Brillouin zone, as plotted in Fig. 4 of the main text and Fig. S17 of the Supplementary Information, with the theory shown here.

For a group of N magnetic subbands with a finite Chern number $C \neq 0$ and separated from the rest of the spectrum by an energy gap, we define the multiband quantum geometric tensor:

$$\eta_{\mu\nu}^{mn}(\mathbf{k}) = N\mathcal{A}\langle\partial_\mu u_{m,k}|[1 - P(\mathbf{k})]|\partial_\nu u_{n,k}\rangle,$$

where $\partial_\mu \equiv \partial_{k_\mu}$ is the derivative with respect to the magnetic wavevector \mathbf{k} , $\langle \mathbf{r} | u_{n,k} \rangle \equiv \langle \mathbf{r} | e^{-i\mathbf{k} \cdot \mathbf{r}} | \Gamma_{n,k} \rangle$ is the periodic part of the mean-field eigenstates, $P(\mathbf{k}) = \sum_{n=1}^N |u_{n,k}\rangle\langle u_{n,k}|$ is the projector onto this group of magnetic subbands, and \mathcal{A} is the area of the magnetic Brillouin zone. The Berry connection and quantum geometric tensor can also be derived from the appropriate action of the position operator on the magnetic translation group irreps [6].

The symmetric and antisymmetric part of the quantum geometric tensor,

$$g_{\mu\nu}^{mn} = \frac{1}{2}(\eta_{\mu\nu}^{mn} + \eta_{\nu\mu}^{mn}), \mathcal{F}^{ab} = i(\eta_{xy}^{mn} - \eta_{yx}^{mn}),$$

are used to formulate the ideal quantum geometry indicators [7]. Considering the gate-screened short range interaction, this is related to the possibilities of hosting fractionalized states; while longer range interactions can change this. Specifically, we define:

$$\sigma[\mathcal{F}] \equiv \text{Tr} \left[\left(\frac{1}{2\pi C} \mathcal{F} - 1 \right)^2 \right]^{\frac{1}{2}} \text{ where } \text{Tr}[O] \equiv \frac{1}{N\mathcal{A}} \sum_{n=1}^N \int d^2\mathbf{k} O_{nn}(\mathbf{k}).$$

The deviation of $\sigma[\mathcal{F}]$ from 0 provides a measure of the Berry curvature uniformity in the magnetic Brillouin zone. We also define the trace condition:

$$T[\eta] \equiv \text{Tr}(g) - |\text{Tr}(\mathcal{F})| \geq 0, g \equiv g_{xx} + g_{yy}.$$

Deviation of $T[\eta]$ from 0 provides a measure of how different the wavefunctions are to those of the lowest Landau level (LLL).

Numerically, $\mathcal{F}(\mathbf{k})$ can be computed by forming an infinitesimal closed loop near k :

$$\mathcal{F}(\mathbf{k}) \approx -\text{Im} \log \left[\hat{\Lambda}_{\mathbf{q}_x}(\mathbf{k}) \hat{\Lambda}_{\mathbf{q}_y}(\mathbf{k} + \mathbf{q}_x) \hat{\Lambda}_{-\mathbf{q}_x}(\mathbf{k} + \mathbf{q}_x + \mathbf{q}_y) \hat{\Lambda}_{-\mathbf{q}_y}(\mathbf{k} + \mathbf{q}_y) \right].$$

Here $[\hat{\Lambda}_{\mathbf{q}}(\mathbf{k})]_{mn} = \langle u_{n,k} | u_{m,k+\mathbf{q}} \rangle$ is the structure factor matrix defined with respect to the group of (interaction-renormalized) subbands of interest, and not to be confused with the non-interacting structure factor defined in previous section. This procedure is inherently gauge-invariant. Similarly, $g(\mathbf{k})$ can be computed by noting that:

$$[\hat{\Lambda}_{\mathbf{q}}(\mathbf{k}) \hat{\Lambda}_{-\mathbf{q}}(\mathbf{k} + \mathbf{q})]_{mn} \approx \delta_{mn} - \sum_{\mu\nu} \mathbf{q}_\mu \mathbf{q}_\nu g_{\mu\nu}^{mn}(\mathbf{k})$$

whose trace is gauge-invariant. In Fig. 4 of the main text and Fig. S17 of the Supplementary Information, we plot the Berry curvature and quantum metric in the magnetic Brillouin zone for

the relevant magnetic subband hosting the experimentally observed FQH. In these plots, q_M is defined following $q_M \equiv \sqrt{|\mathbf{g}_1||\mathbf{g}_2|}/q$ at flux ratio $\Phi/\Phi_0 = p/q$.

A comparison with calculations done for the non-interacting magnetic subband near CNP (Fig. S18) shows that the strong Coulomb interaction improves the uniformity of the Berry curvature (and quantum geometry) of the magnetic subbands even in the presence of substantial heterostrain.

Perturbation from proximitized spin-orbit coupling

The adjacent WSe₂ can induce a combination of two types of SOC in the MATBG (Ising and Rashba):

$$H_{SOC} = \frac{1}{2}\lambda_I\tau_z s_z + \frac{1}{2}\lambda_R(\tau_z\sigma_x s_y - \sigma_y s_x),$$

where τ, σ, s represent the Pauli matrix for valley, sublattice and spin, and λ_I, λ_R are the Ising and Rashba SOC energy scales. The energy scale of the induced SOC was recently found to be dependent on the alignment of the WSe₂ and the adjacent graphene layer: they can be as large as ≈ 2 meV when aligned [8], and close to zero when misaligned. We do not have microscopic information about this twist angle in our device as a prior. Here we consider the largest energy scales obtained in recent experiments $\lambda_I = 1.6$ meV and $\lambda_R = 2$ meV. In Fig. S13, we show the calculated phase diagram with the presence of SOC, at twist angle of 1.05°. The obtained phase diagram is consistent with the phase diagram presented in the main text without SOC.

In below, we presented a brief explanation of the minimum perturbation from the SOC, to both the HF phase diagram and the quantum geometry of the magnetic subbands at high field.

We note that both of the Ising and Rashba SOC energy scale are much smaller compared with the bandwidth of the interacting Hofstader subbands, therefore can be treated using perturbation theory. All phases obtained in our Hartree-Fock calculation are diagonal in spin, i.e. they show no spin-coherence. We separate the discussion of Ising SOC and Rashba SOC.

The Ising SOC induces an energy perturbation that can be understood as a valley contrasting spin Zeeman energy independent of momentum k . As a result, Ising SOC preserves the band dispersion for the Chern insulators with spin and valley polarization at high magnetic field. Moreover, Ising SOC commutes with the Hartree-Fock order parameter and does not alter the band dispersion of the bands. It is therefore straightforward to see that Ising SOC does not perturb the phase diagram from Hartree-Fock calculation in the leading order, and the quantum geometry properties of the FQH parent bands remain unchanged.

For the Rashba SOC, the leading order change to the wavefunction can be written:

$$|\psi_n(k)\rangle \rightarrow |\psi_n(k)\rangle + |\delta\psi_n(k)\rangle, |\delta\psi_n(k)\rangle = \sum_{m \neq n} |\psi_m(k)\rangle \frac{\langle\psi_m(k)|H_R|\psi_n\rangle}{\Delta_{mn}(k)}$$

Where $\Delta_{mn}(k)$ is the direct gap (at momentum k) set by spontaneous symmetry breaking (and enlarged to leading order by Zeeman splitting) which is much larger than λ_R (in our numerics, by a factor of 5- 10). The wavefunction modulation $|\delta\psi_n(k)\rangle$ is in the order of $O(\frac{\lambda_R}{\Delta_{mn}})$ which is about or below 10%. However, we will now show that the Berry curvature and quantum metric are completely unchanged by this wavefunction correction due to a spin-symmetry selection rule.

For the quantum geometry, we consider the parent band of FQH states $|\psi_n(k)\rangle$ which are valley and spin polarized. This means that $\langle\psi_m(k)|H_R|\psi_n\rangle$ is nonzero only for m being the opposite spin and same valley. Thus $|\delta\psi_n(k)\rangle$ is always spin-polarized in the opposite direction as $|\psi_n(k)\rangle$. The Berry curvature \mathcal{F} changes under this wavefunction perturbation via

$$\mathcal{F} = i\epsilon_{ij}\partial_i\langle\psi_n(k)|\partial_j|\psi_n(k)\rangle \rightarrow \mathcal{F} + \delta\mathcal{F}$$

where ∂_j is the momentum derivative and the leading order correction $\delta\mathcal{F}$ is

$$\delta\mathcal{F} = i\epsilon_{ij}\partial_i\langle\psi_n(k)|\partial_j|\delta\psi_n(k)\rangle + i\epsilon_{ij}\partial_i\langle\delta\psi_n(k)|\partial_j|\psi_n(k)\rangle = 0$$

because $\partial|\delta\psi_n(k)\rangle$ and $\partial|\psi_n(k)\rangle$ are supported on different spin Hilbert spaces and have zero overlap. The Fubini-Study metric, or quantum metric, g can be written in terms of the projector $P(k) = |\psi_n(k)\rangle\langle\psi_n(k)|$ as $g = \frac{1}{2}Tr(\partial P)^2$, so we find

$$\delta g(k) = Tr \partial_i P \partial_i \delta P = 0$$

which also vanishes identically because δP and P are block diagonal for all k in spin space, but are supported entirely on opposite spin sectors.

Note S3. Orbital decomposition of the magnetic subbands

An alternative way of interpreting the FQHs is to make analogies to the single LL physics of a monolayer graphene. We can express the magnetic subband wavefunctions in terms of the monolayer LL wavefunctions. Specifically for the Landau gauge used here, we denote the monolayer LL wavefunction as $|\psi_{Nl,r}^{(\eta s)}(k_2)\rangle$, where $l = t, b$ is the layer index and $N = 0, \pm 1, \pm 2, \dots$ is the LL index. In above notation we replaced the quantum number $k_y \in (-\infty, \infty)$ by:

$$k_y = \frac{2\pi}{|L_2|} \left(k_2 + r \frac{1}{q} \right), k_2 \in [0, 1/q], r \in \mathbb{Z},$$

yielding a consistent definition of k_2 as previously where it is used to denote the quantum number within the first magnetic Brillouin zone. We refer interested readers to Ref. [1] SI Sec.

II for a detailed derivation. The single-electron eigenstates $|\Gamma_{n,\mathbf{k}}\rangle$ of the Hartree-Fock Hamiltonian can be expressed as:

$$|\Gamma_{n,\mathbf{k}}\rangle = \sum_{\eta s, Nlr} \tilde{U}_{\eta s Nlr, n}(\mathbf{k}) \left| \psi_{Nl,r}^{(\eta s)} \left(k_2 + r \frac{1}{q} \right) \right\rangle.$$

where $\tilde{U}_{\eta s Nlr, n}(\mathbf{k})$ is a unitary matrix at every \mathbf{k} from the Hartree-Fock calculations. It relates the single-electron eigenstates to the monolayer LL wavefunctions. The orbital decomposition of the magnetic subband (n_0) relevant for the experimentally observed FQHs can therefore be calculated as:

$$W_N^{(n_0)} = \sum_{\eta s, lr, \mathbf{k}} |\tilde{U}_{\eta s Nlr, n}(\mathbf{k})|^2.$$

If the FQH is born out of single LL physics, then we expect the orbital decomposition to be strongly peaked at a single LL index N . In Figure S16, we show that the relevant magnetic subband mixes many LLs, and therefore inconsistent with FQH emerging from a single LL.

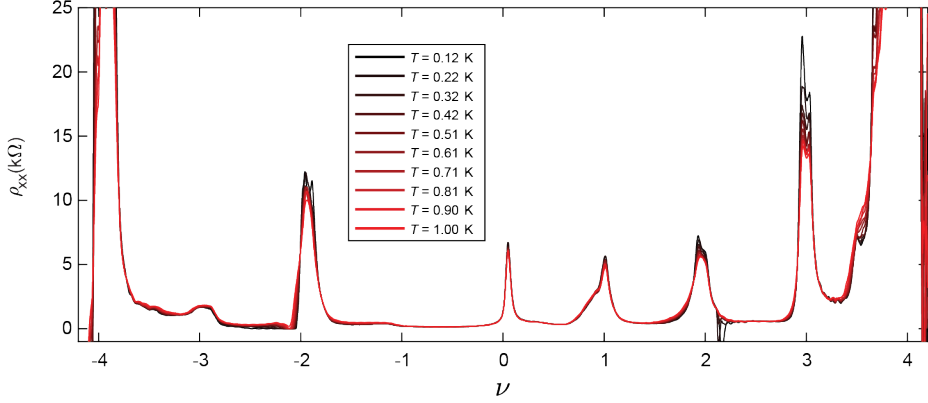


Figure S1. Temperature dependence of the resistivity ρ_{xx} at zero magnetic field. At integer filling factors within the flat bands, we observe weakly insulating states at $\nu = -2, 2, 3$. The resistive peak at $\nu = -3, 0, 1$ is nearly temperature independent below 1 K. No resistive peak is observed for $\nu = -1$.

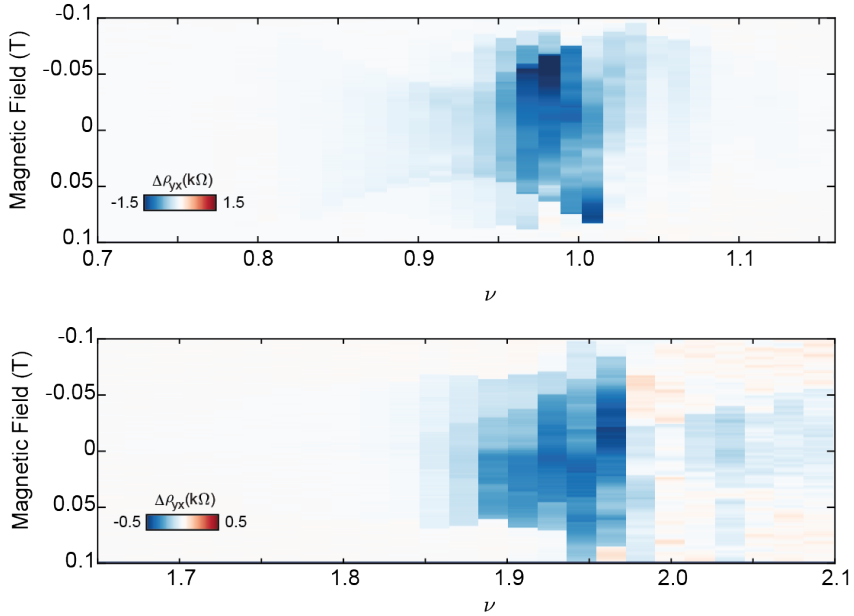


Figure S2. Filling factor dependence of AHE near $\nu = 1$ and 2. The ν dependence of the AHE near $\nu = 1$ and 2 are shown in top and bottom panels respectively. We plot the amplitude of the hysteresis loop in Hall resistivity, $\Delta\rho_{yx} = \rho_{yx}^{B\downarrow} - \rho_{yx}^{B\uparrow}$.

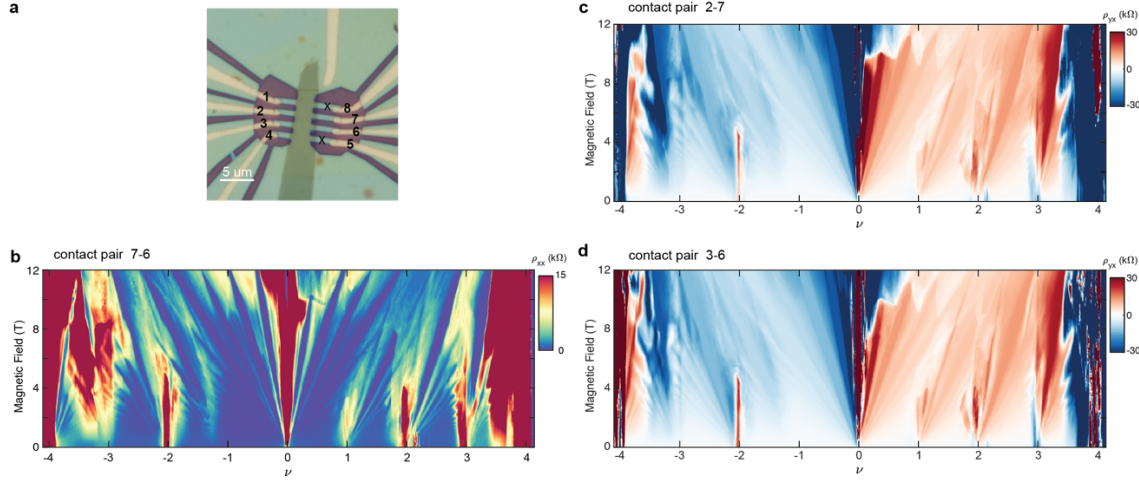


Figure S3. Landau Fan diagram in Hall resistivity ρ_{yx} and other contact pairs. **a**, Optical image of the MATBG device in this study. The contacts are labelled with numbers. Contacts marked with ‘X’ are not conducting due to fabrication issues. **b**, Resistivity ρ_{xx} measured using another contact pair 7-6. Data shown in Fig.2 and Fig.4 are from this contact pair. **c-d**, Hall resistivity ρ_{yx} using contact pair 2-7 and 3-6 respectively. For measurements at $\nu > 0$ ($\nu < 0$), the graphene contacts are slightly electron (hole) doped to achieve optimal quality.

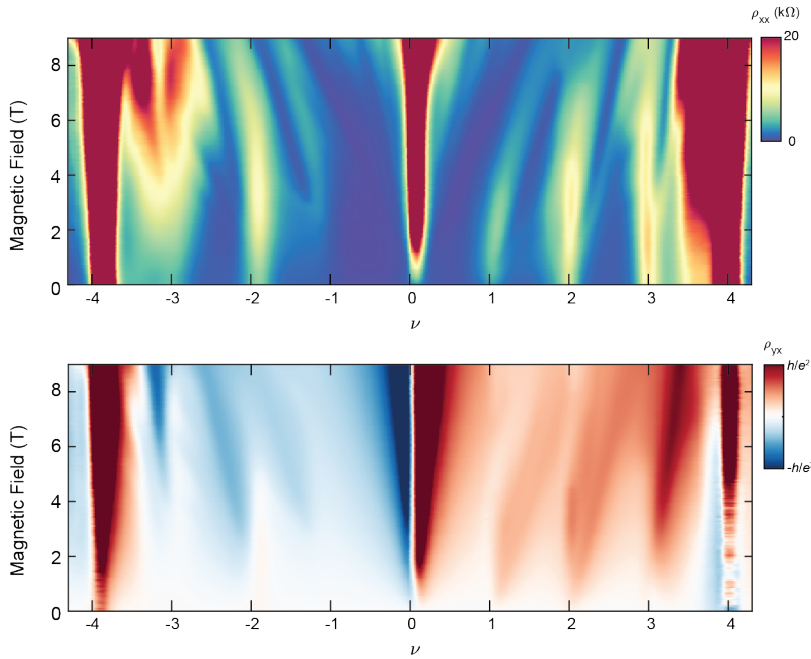


Figure S4. Landau Fan diagrams in ρ_{xx} and ρ_{yx} at $T = 2$ K. At high temperature, correlated states with larger energy gaps survive. In particular, we note the observation of the main sequence correlated Chern insulators (CCI) with total Chern number $|t| = 1, 2, 3$ and moiré filling factor $|s| = 3, 2, 1$, as well as the integer quantum Hall (IQH) state with $|t| = 4$.

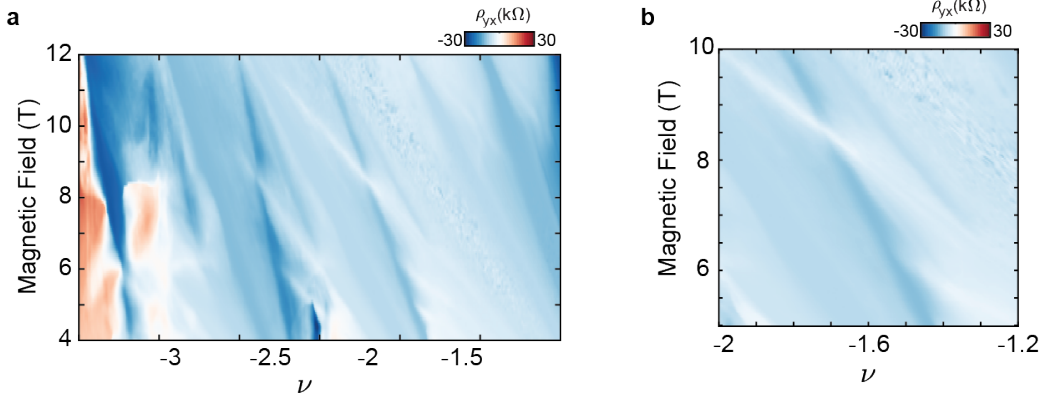


Figure S5. Landau Fan diagrams in ρ_{yx} of the SBCIs. Zoom-in measurement of the ρ_{yx} Landau fan focusing on the SBCI states on the hole-doped side. **a** and **b** panels show ρ_{yx} in the same phase space as shown in Fig. 2a and c.

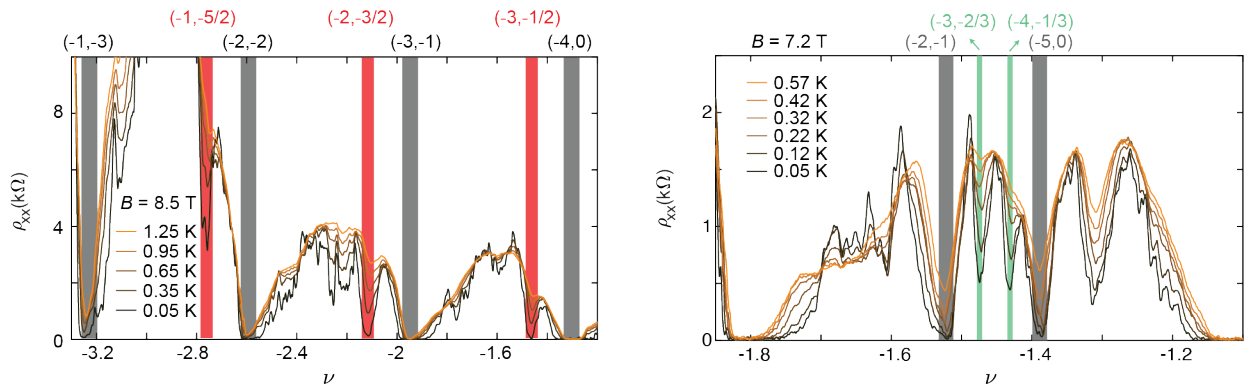


Figure S6. Temperature dependence of the SBCIs. The suppressed resistivity ρ_{xx} at low temperature show the clear formation of the SBCIs, marked by the red and green shaded regions.

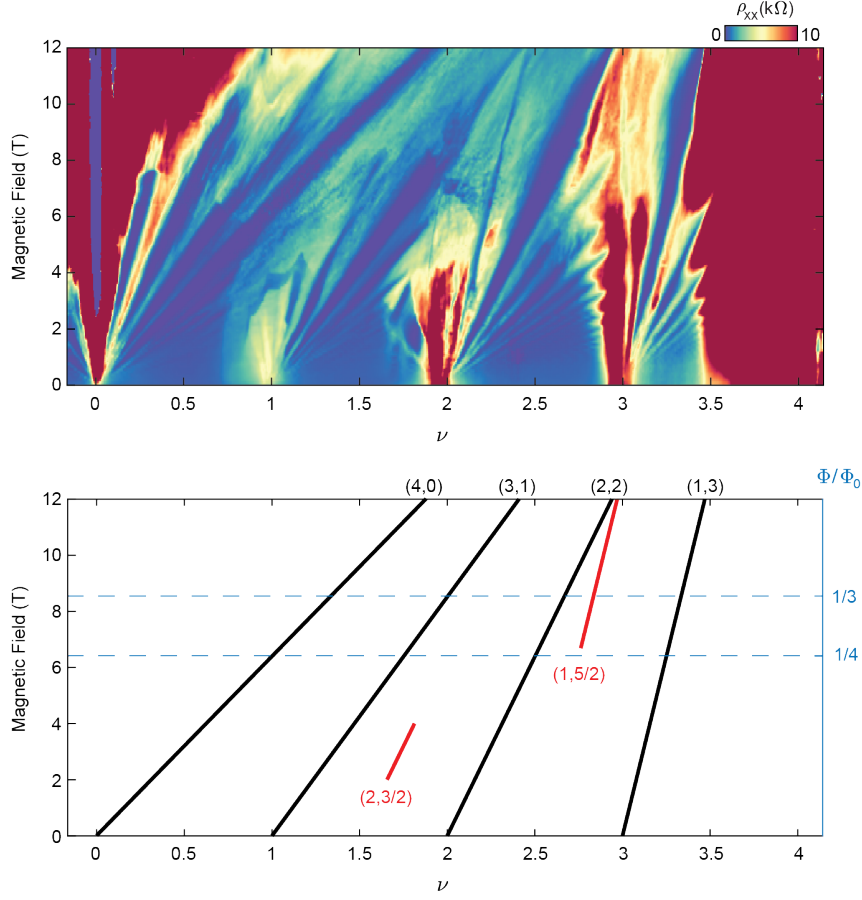


Figure S7. Observation of SBCIs at electron doping side. Landau fan diagram in resistivity ρ_{xx} measured at $T = 300$ mK, focusing on the phase space $\nu > 0$. Although a similar cascade of SBCI states is naively expected on the electron doping side in the presence of approximate particle-hole symmetry, we do not see this in our Landau fan. At high magnetic field, we only observe a weak $(1, 5/2)$ SBCI state within this sequence. The $(2, 3/2)$ and $(3, 1/2)$ states were previously reported but are absent here. However, the $(2, 3/2)$ SBCI is observed over a small range of magnetic field between $\approx 2 - 3$ T nearby the correlated insulator at $\nu = 2$. It is currently not clear why the electron-doped side of our sample deviates from the behavior of the hole-doped side, as well as from prior samples and theoretical expectation.

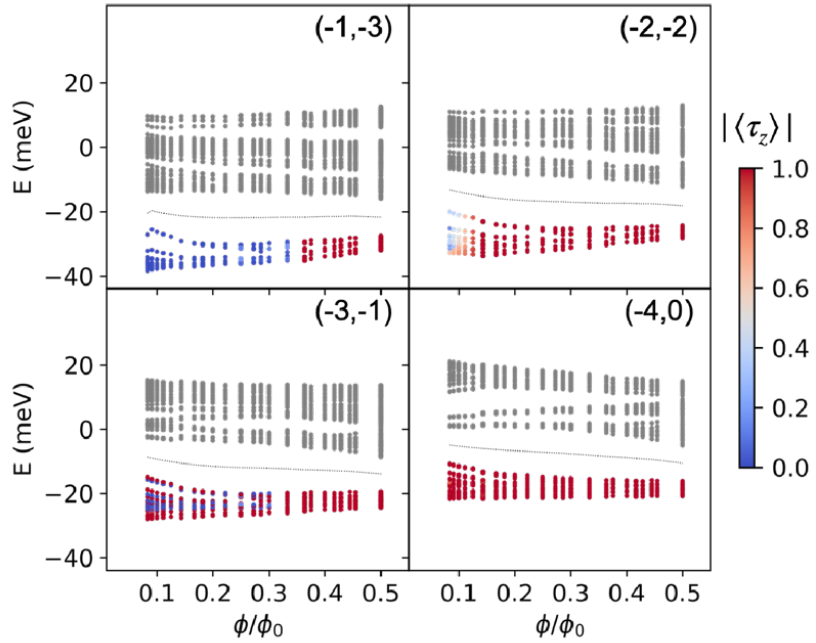


Figure S8. Flavor symmetry of the main sequence Correlated Chern insulators with $(t, s) = (-1, -3), (-2, -2), (-3, -1)$. The valley and spin symmetric IQH along $(-4, 0)$ is plotted for reference. The occupied states are colored by their valley polarization $\langle \tau_z \rangle$. $\langle \tau_z \rangle \rightarrow 1$ means maximal valley polarization whereas $\langle \tau_z \rangle \rightarrow 0$ means maximal intervalley mixing. For $(-1, -3), (-2, -2), (-3, -1)$, the CCIs experience a phase transition from a correlated Hofstadter ferromagnet (CHF) at high magnetic field to an IKS state at low magnetic field. Figure reproduced from Ref. [1] SI.

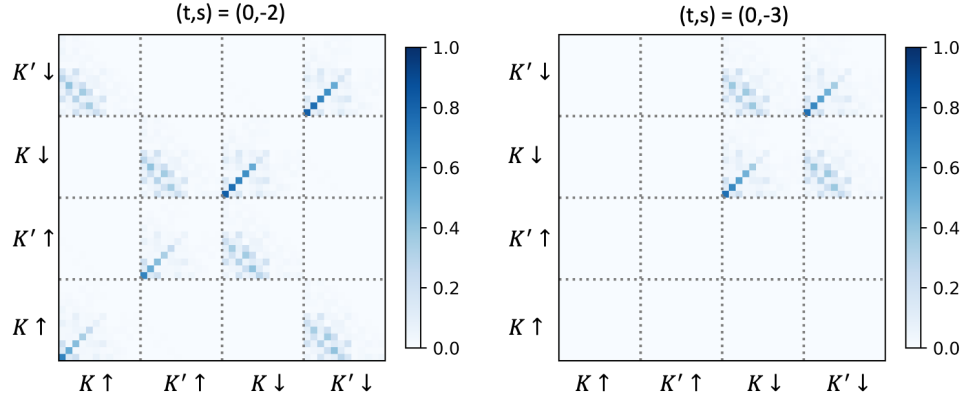


Figure S9. Flavor symmetry of the $t = 0$ IKS states at finite magnetic field. Representative density matrices (absolute value) at Γ point of the magnetic Brillouin zone for: left panel, (0,-2); right panel, (0,-3) IKS states respectively. Calculation is done at $\Phi/\Phi_0 = 1/6$. For the heterostrain we used in the calculation, the IKS wavevector is $\mathbf{Q}_{IKS} = \mathbf{g}_1/2$. We caution however that the \mathbf{Q}_{IKS} can change subject to uniaxial heterostrain condition in relevant experiments.

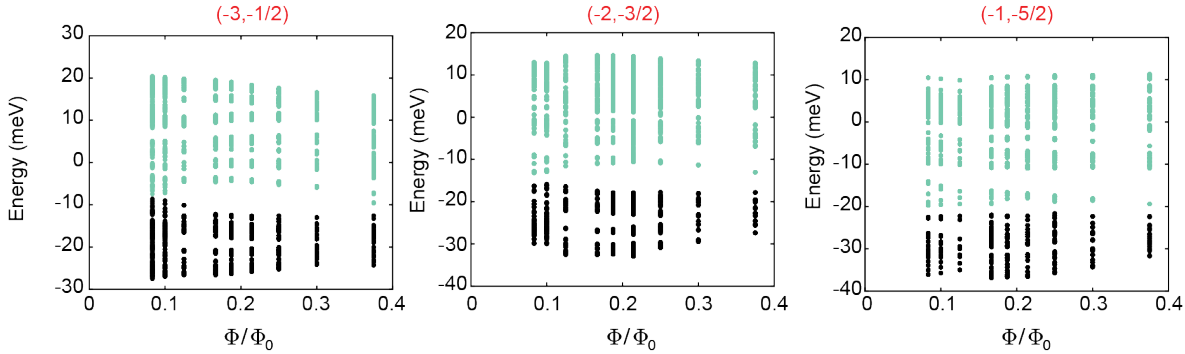


Figure S10. Interacting Hofstadter spectrum of the half-integer SBCIs. Energy spectra vs flux are calculated when the Fermi energy is within the gap of the three half-integer SBCIs. We use the same color scheme as in Fig. 3 to denote the occupied (green) and unoccupied (black) states.

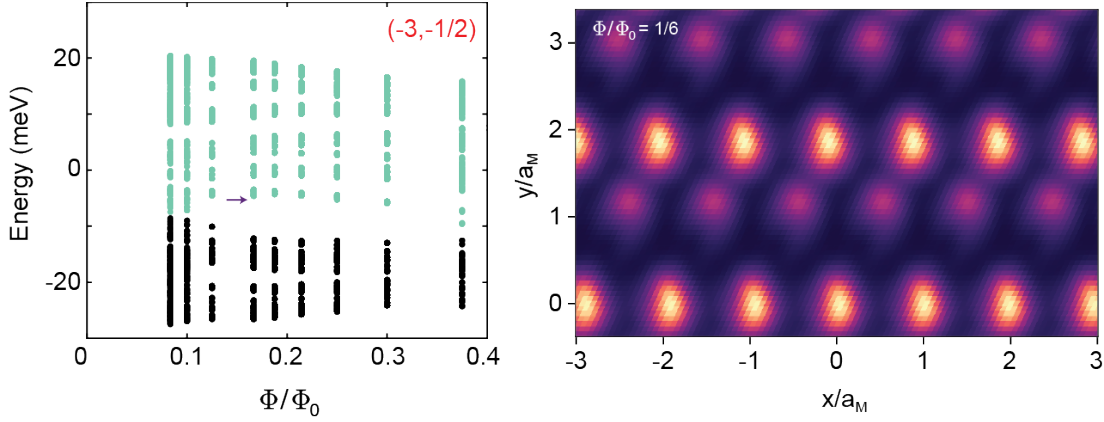


Figure S11. Local density of states at the conduction band edge of the $(-3, -1/2)$ SBCI.
 Calculation is done at $\Phi/\Phi_0 = 1/6$, pointed out by the purple arrow in the left energy spectrum.
 a_M ($a_M \equiv \sqrt{|\mathbf{L}_1||\mathbf{L}_2|}$) is the effective periodicity of the strained moiré superlattice. The stripe-like charge density distribution breaks the moiré translation symmetry, similar to that at the valence band edge of the SBCI in Fig. 3 of the main text.

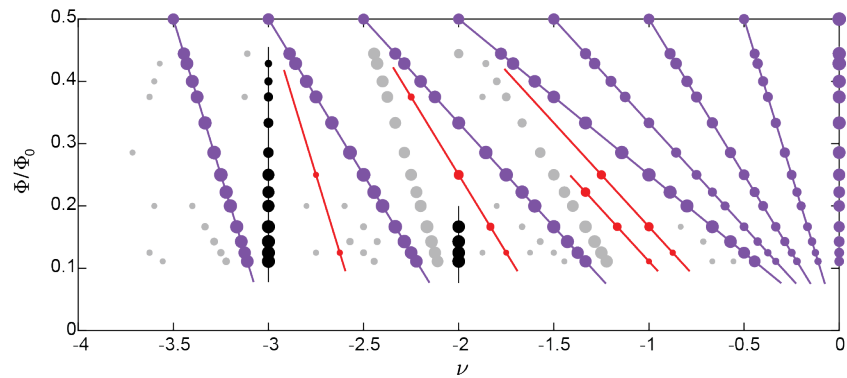


Figure S12. Finite-field Hatree-Fock calculation at twist angle 1.03° . Calculated gapped states at finite magnetic field, at twist angle of 1.03° , which is the actual twist angle of the our sample. The marker size is proportional to the gap size at each filling factor ν and magnetic flux ratio Φ/Φ_0 . The color schematic follows that of Figure 3. The finite field HF phase diagram is consistent with calculation at 1.05° presented in the main text.

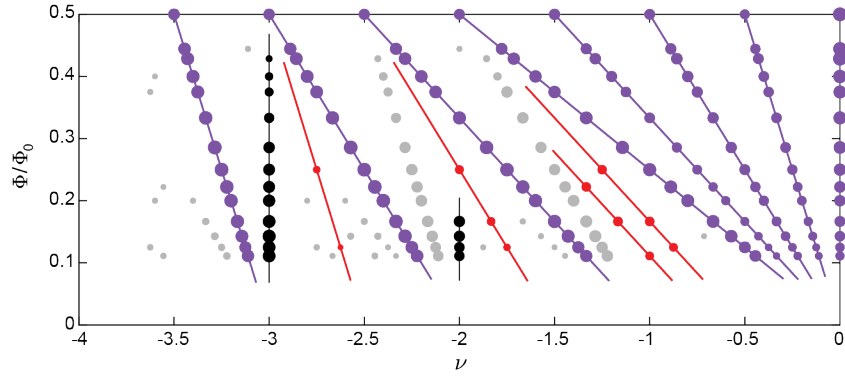


Figure S13. Finite-field Hartree-Fock calculation at twist angle 1.05° with presence of SOC.
 Calculated gapped states at finite magnetic field, at twist angle of 1.05° with presence of spin orbital coupling, $\lambda_I = 1.6 \text{ meV}$, $\lambda_R = 2 \text{ meV}$. The marker size is proportional to the gap size at each filling factor ν and magnetic flux ratio Φ/Φ_0 . The color schematic follows that of Figure 3. The finite field HF phase diagram is unchanged by the perturbation of a small SOC proximitized by the WSe₂ layer.

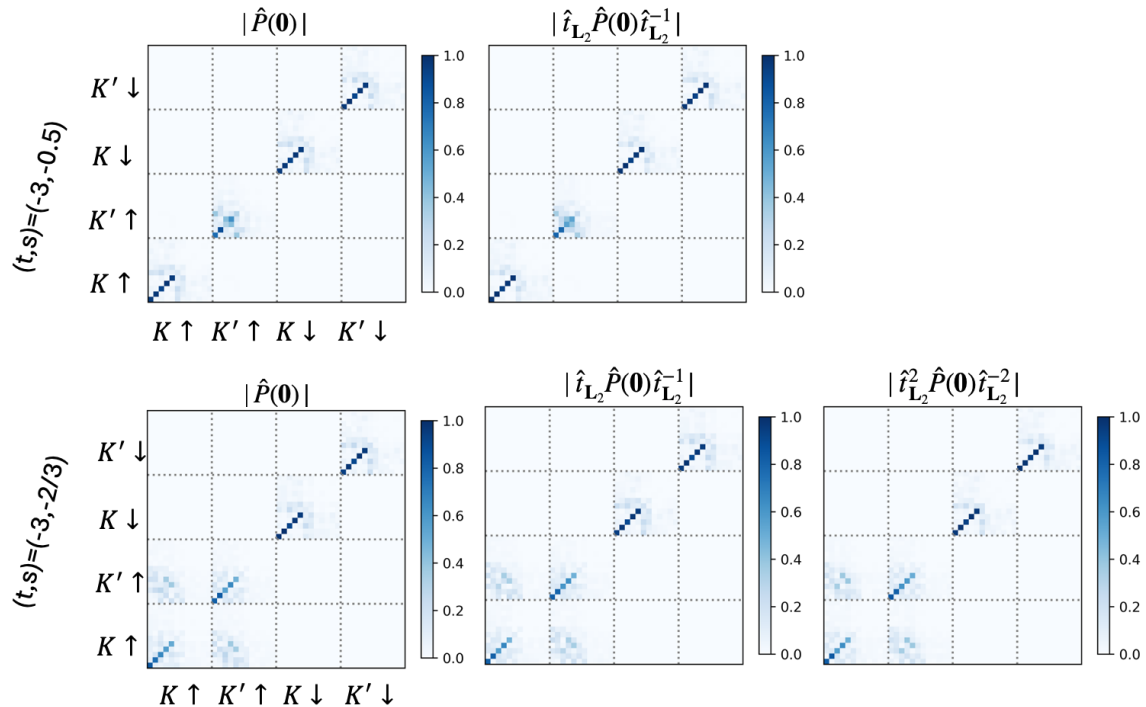


Figure S14. Flavor and magnetic translation symmetry of SBCI states at finite magnetic field.
 Representative density matrices (absolute value) at a few magnetic wavevectors for: upper panel, $(t, s) = (-3, -1/2)$; lower panel, $(-3, -2/3)$ SBCI states respectively. Calculation is done at $\Phi/\Phi_0 = 1/6$. The period of the stripe is identified via \hat{t}_{L_2} translations. For $(-3, -1/2)$, the density matrix repeats upon $\hat{t}_{L_2}^2$, corresponding to a period - 2 stripe. For $(-3, -2/3)$ it is a period - 3 stripe.

The SBCI states can be either valley and spin polarized (upper panel) or developing intervalley coherence (lower panel). However, due to the small Hartree-Fock energy differences (~ 0.05 meV per moiré unit cell), we do not postulate if either type of SBCIs will be observed in experiments.

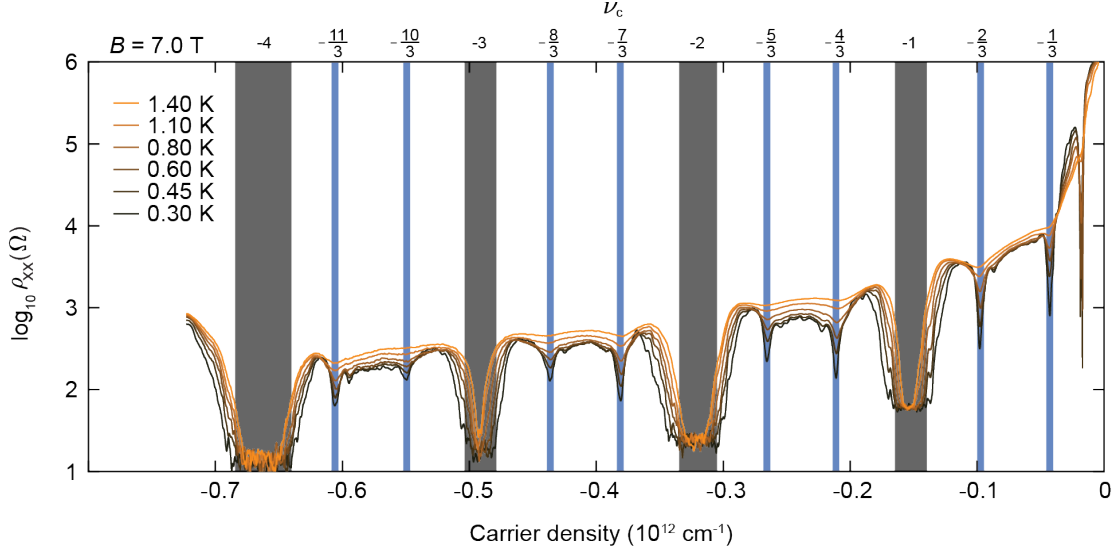


Figure S15. Temperature dependence of the FQHs. Resistivity ρ_{xx} of the FQHs measured at $B = 7$ T and various temperature, in log scale. The FQHs with denominator 3 is marked by the blue shaded region, where we obtain the thermal activation gap as shown in Fig. 4b inset.

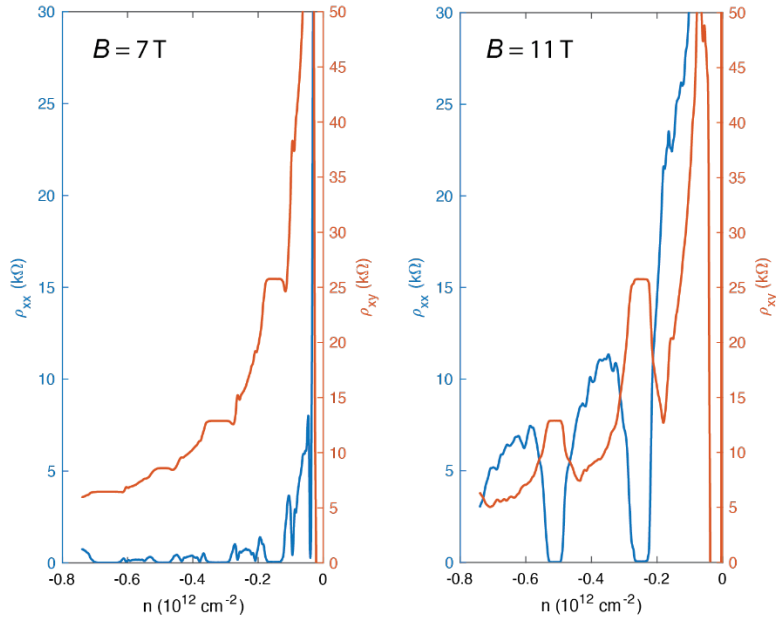


Figure S16. FQHs and Fermi liquid at high magnetic field. Resistivity ρ_{xx} and Hall resistivity ρ_{xy} of the FQHs measured at $B = 7$ T and 11 T. At high magnetic field, the FQH states disappear and transition into a dissipative Fermi liquid phase at partial fillings of the magnetic subbands.

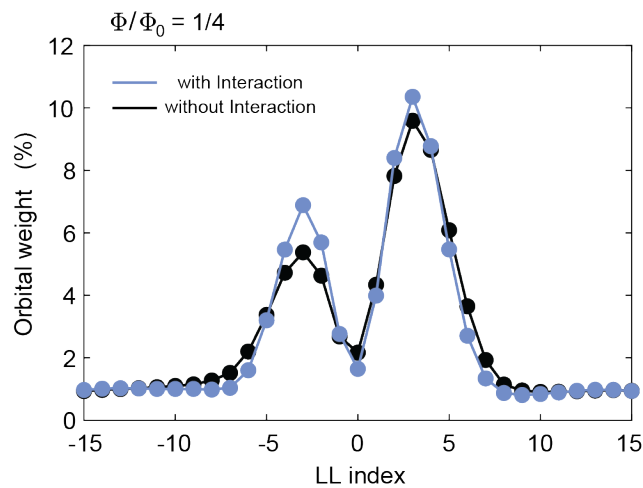


Figure S17. Orbital decomposition of the magnetic subband. Decomposition of the FQH's parent magnetic subband, in both the interacting Hofstadter spectrum (blue) and the non-interacting single-particle Hofstadter spectrum (black). In both cases, the magnetic subband has strong orbital weight at high N LLs peaked at $N = 3$ and -3. The Coulomb interaction reduces the number of LL mixings, pushing the subband wavefunctions closer to that of a higher N LL.

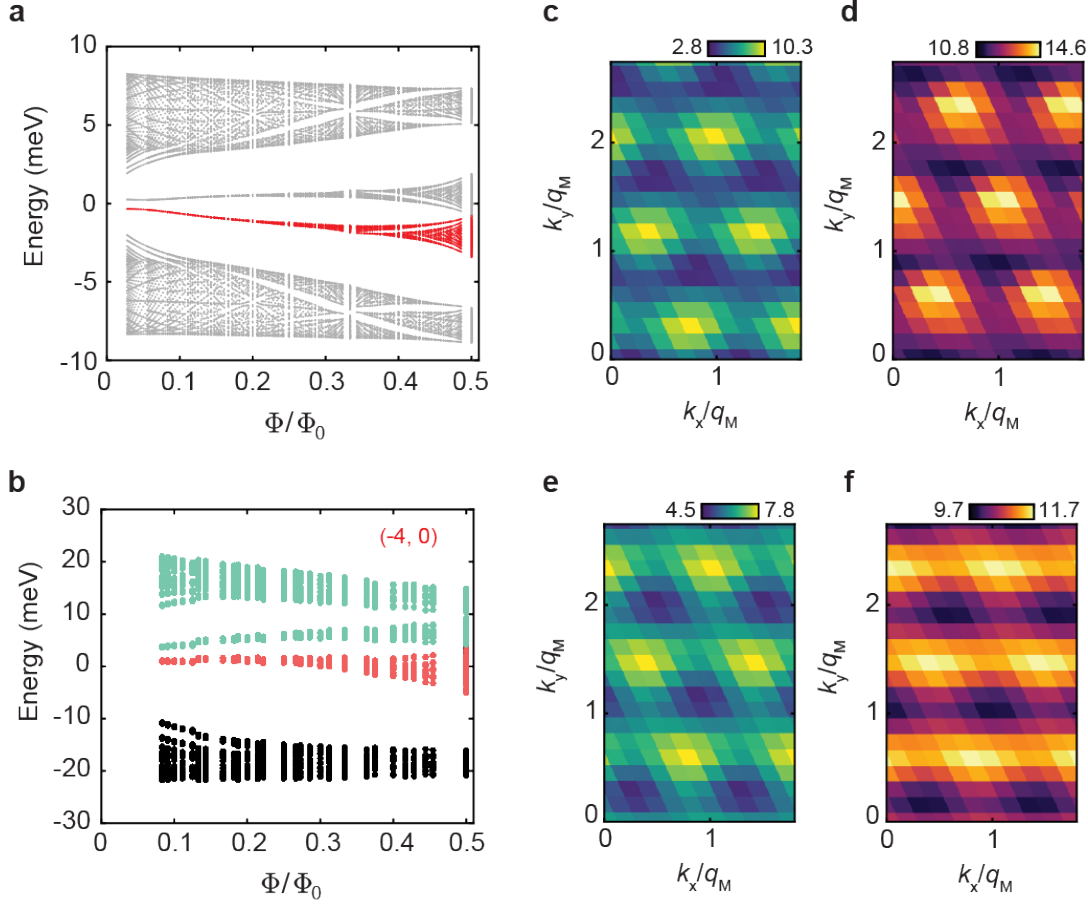


Figure S18. Comparison of the quantum geometry conditions with and without Coulomb interaction. **a-b**, Non-interacting Hofstadter spectrum and interacting Hofstadter spectrum (Fermi energy within (-4,0) IQH gap) respectively, both plotted for the K valley with spin down. The parent subbands of the FQHs are marked red. The Coulomb interaction significantly broaden the bandwidth of that from a single-particle calculation. **c-d**, Berry curvature \mathcal{F} and quantum metric g of the non-interacting subband respectively, calculated at $\Phi/\Phi_0 = 1/4$. **e-f**, Berry curvature \mathcal{F} and quantum metric g of the interacting subbands respectively, calculated at $\Phi/\Phi_0 = 1/4$. q_M is defined following $q_M \equiv \sqrt{|\mathbf{g}_1||\mathbf{g}_2|}/q$ at flux ratio $\Phi/\Phi_0 = p/q$. Absolute values of \mathcal{F} and g are plotted instead of normalized values. Except for the spatial shift of the \mathcal{F} and g hotspot, we highlight that the spatial distribution of the interacting subband is much smoother compared with the non-interacting subband.

Reference

- [1] Xiaoyu Wang and Oskar Vafek, Theory of correlated Chern insulators in twisted bilayer graphene. *Phys. Rev. X* **14**, 021042 (2024).
- [2] Biao Lian, Zhijun Wang, and B. Andrei Bernevig, Twisted Bilayer Graphene: A Phonon-Driven Superconductor, *Phys. Rev. Lett.* **122**, 257002 (2019)
- [3] Zhen Bi, Noah F. Q. Yuan, and Liang Fu, Designing flat bands by strain, *Phys. Rev. B* **100**, 035448 (2019)
- [4] Y. H. Kwan, G. Wagner, T. Soejima, M. P. Zaletel, S. H. Simon, S. A. Parameswaran, and N. Bultinck, Kekulé Spiral Order at All Nonzero Integer Fillings in Twisted Bilayer Graphene, *Phys. Rev. X* **11**, 041063 (2021).
- [5] Dumitru Călugăru, Nicolas Regnault, Myungchul Oh, Kevin P. Nuckolls, Dillon Wong, Ryan L. Lee, Ali Yazdani, Oskar Vafek, and B. Andrei Bernevig, Spectroscopy of Twisted Bilayer Graphene Correlated Insulators, *Phys. Rev. Lett.* **129**, 117602 (2022)
- [6] Jonah Herzog-Arbeitman, Aaron Chew, and B. Andrei Bernevig, Magnetic Bloch theorem and reentrant flat bands in twisted bilayer graphene at 2π flux, *Phys. Rev. B* **106**, 085140 (2022).
- [7] Rahul Roy, Band geometry of fractional topological insulators, *Phys. Rev. B* **90**, 165139 (2014).
- [8] Yiran Zhang, Gal Shavit, Huiyang Ma, Youngjoon Han, Kenji Watanabe, Takashi Taniguchi, David Hsieh, Cyprian Lewandowski, Felix von Oppen, Yuval Oreg, Stevan Nadj-Perge, Twist-Programmable Superconductivity in Spin-Orbit Coupled Bilayer Graphene. arXiv:2408.10335 (2024).